# Excitation strings and topological surgery in artificial spin ice

Xiaoyu Zhang<sup>1,2,3</sup>, Ayhan Duzgun<sup>4</sup>, Yuyang Lao<sup>2,3</sup>, Nicholas S. Bingham<sup>1</sup>, Joseph Sklenar<sup>2,3,5</sup>, Hilal Saglam<sup>1</sup>, Shayaan Subzwari<sup>1</sup>, Joseph T. Batley<sup>6</sup>, Justin D. Watts<sup>6,7</sup> Daniel Bromley<sup>8</sup>, Chris Leighton<sup>6</sup>, Liam O'Brien<sup>8</sup>, Cristiano Nisoli<sup>4</sup>, & Peter Schiffer<sup>1,2,3,9</sup>

<sup>1</sup>Department of Applied Physics, Yale University, New Haven, CT 06511, USA

<sup>2</sup>Department of Physics, University of Illinois at Urbana-Champaign, Urbana, Illinois 61801, USA

<sup>3</sup>Frederick Seitz Materials Research Laboratory, University of Illinois at Urbana-Champaign, Urbana, Illinois 61801, USA

<sup>4</sup>Theoretical Division and Center for Nonlinear Studies, MS B258, Los Alamos National Laboratory, Los Alamos, New Mexico 87545, USA

<sup>5</sup>Department of Physics and Astronomy, Wayne State University, Detroit, Michigan 48201, USA

<sup>6</sup>Department of Chemical Engineering and Materials Science, University of Minnesota, Minneapolis, Minnesota 55455, USA

<sup>7</sup>School of Physics and Astronomy, University of Minnesota, Minneapolis, Minnesota 55455, USA

Bepartment of Physics, University of Liverpool, Liverpool L69 3BX, United Kingdom
Department of Physics, Yale University, New Haven, CT 06511, USA

Systems of interacting nanomagnets known as artificial spin ices are models for exotic behavior due to their accessibility to geometries and measurement modalities that are not available in natural materials 1,2,3,4,5. Despite being fundamentally composed of binary moments, these systems often display collective phenomena associated with emergent higher-order frustration. We have studied the vertex-frustrated Santa Fe ice<sup>6</sup>, examining its moment structure both after annealing near the ferromagnetic Curie point, and in a thermally dynamic state. We experimentally demonstrate the existence of a disordered string ground state, in which the magnetic structure can be understood through the topology of emergent strings of local excitations. We also show that the system can support a long-range-ordered ground state for certain ratios of local interactions. Both states are accessible via moment reversals only through topological surgery,7 i.e., the breaking of pairs of crossed strings and their reattachment in topologically inequivalent configurations. While we observe instances of topological surgery in our experimental data, such events are energetically suppressed, and we find that an apparent kinetic bottleneck associated with topological surgery precludes the system from achieving either ground state through local moment flips. Santa Fe ice thus represents an unusual instance of competition between topological complexity and ordering, suggesting analogous structures in the quantum realm.

Numerous exotic states and emergent phenomena arise from correlations that develop from relatively simple interactions in carefully designed systems with unusual geometries and connectivity. An important class of such systems has recently emerged in artificial spin ice arrays of coupled single-domain nanomagnets<sup>1,2,3,3,4</sup>. While artificial spin ice

research was originally focused on modelling the frustration seen in pyrochlore spin ice materials,<sup>8</sup> the studied phenomena have expanded to include a wide range of exotic behavior such as monopole-like excitations and fractionalization,<sup>3,4</sup> as well as the realization of new geometrically frustrated geometries with unusual and distinct properties. <sup>5,6,9,10,11,12,13,14,15,16,17,18</sup>

Here we report an experimental and theoretical study of an artificial spin ice system of designed topological complexity at the nanoscale, Santa Fe ice (SFI)<sup>6</sup>. The structure of SFI is shown in Figure 1a, where each island in the image is a single-domain nanoscale ferromagnet that behaves like a binary Ising-like moment. Figure 1b shows the structure of one of our experimental samples, and Figures 1c and 1d show experimental measurements of the individual moments in SFI, as described in detail below. The unit cell of SFI, indicated in Figure 1a, is composed of four composite large squares, each composed of eight elementary rectangular plaquettes consisting of six moments – two interior plaquettes and six peripheral plaquettes. Following previous analyses of artificial spin ice systems, we describe SFI in a nearest-neighbor approximation via a vertex-model<sup>19</sup>, i.e., we consider the system through the states of the lattice vertices as defined by the possible configurations of moments at each vertex of the lattice (Figure 2a).

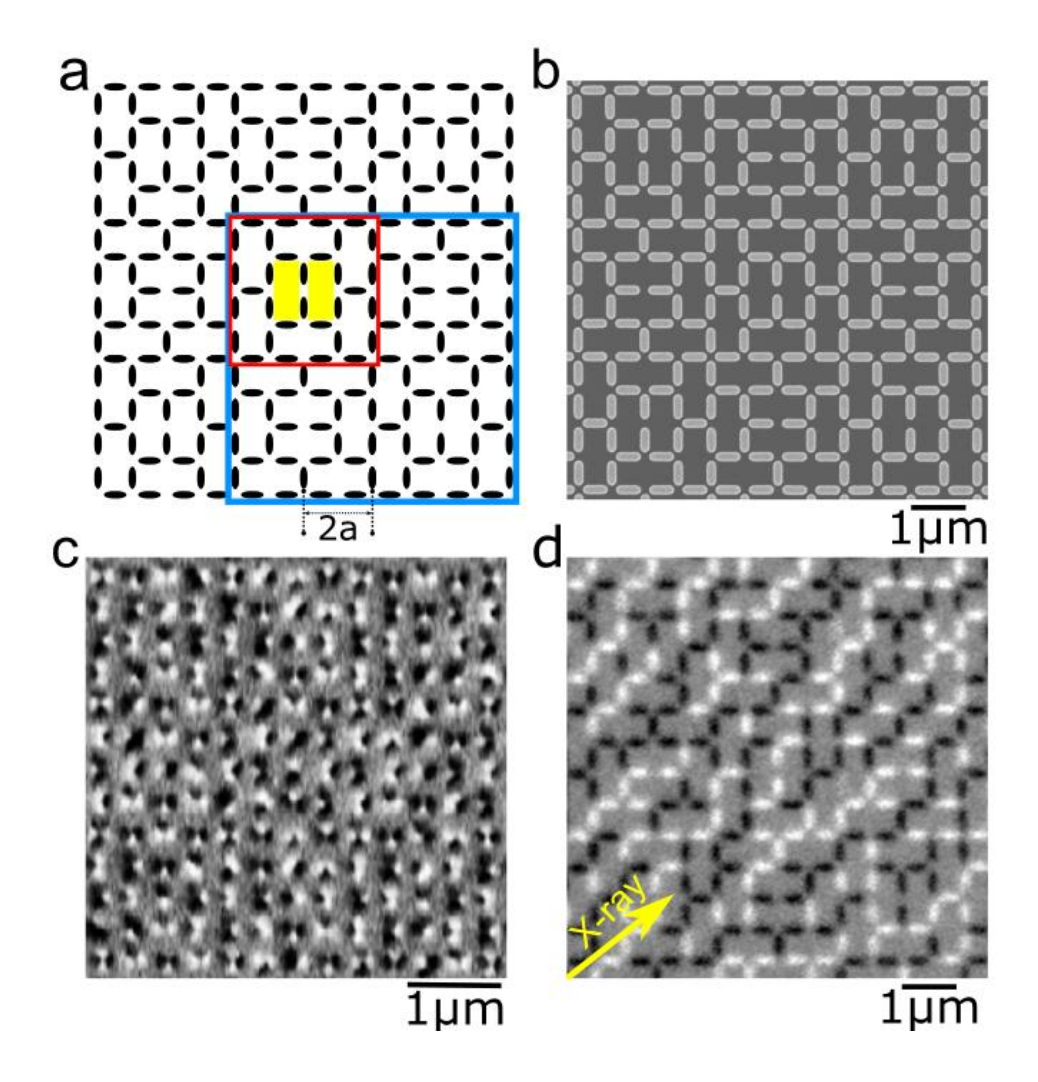


Figure 1: Santa Fe ice (a). Schematic of the Santa Fe ice (SFI) geometry, where each element represents a single-domain nanomagnet, and the lattice constant is *a*. The unit cell (indicated in blue) is made of four composite squares (one of which is indicated in red). Each composite square has eight rectangular plaquettes, which can be categorized as pairs of "interior" plaquettes (indicated by yellow filling) that are separated by a pair of islands, and "peripheral" plaquettes that surround them. (b). Scanning Electron Microscopy (SEM) image of SFI. (c). Magnetic force microscopy (MFM) image of SFI, in which each nanoisland has black and white contrasting ends, indicating the moment poles. (d). Photoemission electron microscopy – x-ray magnetic circular dichroism (PEEM-XMCD) image of SFI, in which the entire islands are either black or white, indicating the magnetic moment direction through its component aligned with the incident x-ray beam (yellow arrow).

Santa Fe ice belongs to the class of "vertex frustrated" artificial spin ices<sup>3,6</sup> in which the moments cannot be arranged such that each vertex is in its local ground state. In other words, the lattice structure of SFI forces some fraction of the vertices to be in an excited state. These excited vertices have been dubbed "unhappy vertices" in previous works<sup>6,20</sup>. Within this framework, the proper description of SFI is not in terms of magnetic moments but rather in terms of the degenerate allocation of such unhappy vertices. In Figure 2a, we show all the possible moment configurations on each vertex type, noting that vertices in this lattice can include either two, three, or four moments, i.e., they can have a coordination number of z = 2, 3 or 4. By definition, an unhappy vertex includes at least one pair of nearest neighbor moments that have an energetically unfavorably mutual orientation.<sup>6</sup> We term each of the plaquettes bordered by such a pair of moments as being "connected" by the unhappy vertex, a concept that we will use below. In Figure 2b, the connected plaquettes are each joined by a line, following a construction first used in understanding the physics of Shakti ice,<sup>11</sup> but applicable to any artificial spin ice based on a square geometry.

Understanding that the two moments in the center of each composite square form a z = 2 vertex, it is straightforward to verify that the each of the interior plaquettes must be connected by an *odd* number of unhappy vertices around its edges. Those plaquettes are therefore intrinsically frustrated in that they cannot have all vertices in a ground state. It is equally easy to verify that each of the peripheral plaquettes must be connected by an *even* number of unhappy vertices (including, possibly, zero). These two conditions are a strict constraint, irrespective of the system temperature: there must be at least one

unhappy vertex connected with each interior plaquette, and there could be zero or any even number on any of the peripheral plaquettes. This property of SFI contrasts with the other well-studied vertex-frustrated geometries, Shakti and Tetris ice, in which each constituent plaquette is connected by at least one unhappy vertex. The peculiarity of the Santa Fe structure is that only the interior plaquettes are necessarily connected by an unhappy vertex, leading to the string dynamics described below.

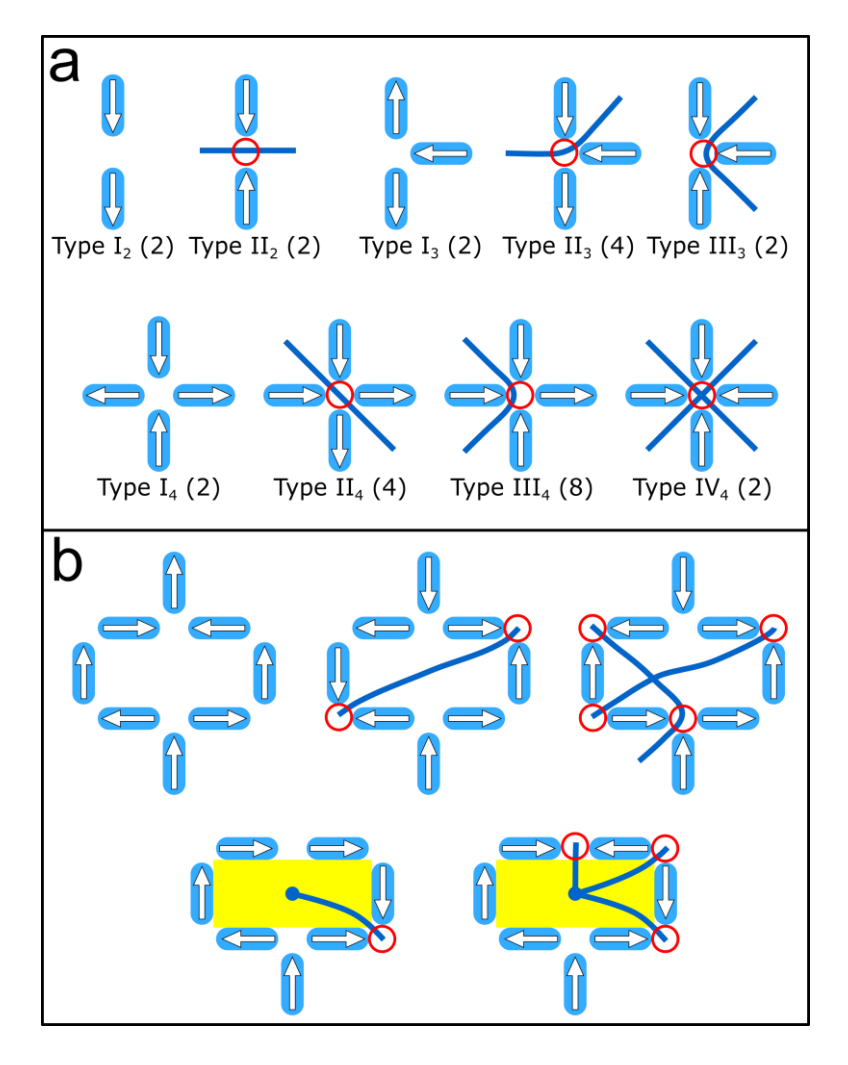


Figure 2: Vertex types and emergent string representation (a). Vertex moment configurations for different vertex coordination numbers, z = 2, 3, and 4, arranged in order of increasing energy, where the arrows indicate moment direction and the red circles denote an excited state of the vertex (i.e., an unhappy vertex). The numbers in parentheses show the degeneracy for each given vertex type. The blue lines represent string segments "connecting" the plaquettes through the unhappy vertices. (b). Examples of moment and string configurations for peripheral and interior (yellow-filled) plaquettes. Because of the SFI lattice geometry, a peripheral plaquette is connected by an even number of unhappy vertices, and an interior plaquette is connected by an odd number.

The constraints described above yield two rather different collective magnetic ground states for the SFI system, a long-range-ordered state and a disordered string state. The long-range-ordered state can be achieved by simply restricting the unhappy vertices to the shared moments of each pair of interior plaquettes, i.e., having all of the z = 2 vertices in the type  $II_2$  state, and all other vertices in their ground state (Figure 3a). This state has the same local moment configuration as observed in the ordered ground state of the artificial square ice lattice, modulo the missing islands.

The disordered string ground state arises when a fraction of the z = 3 vertices are in unhappy states. Geometrically, a z = 3 unhappy vertex that connects an interior plaquette in SFI must also connect a peripheral plaquette. In order to yield an even number of unhappy vertices for that peripheral plaquette, a second unhappy vertex must then also be connected to it. That vertex in turn connects to another peripheral plaquette, and it is thus natural to visualize their connectivity as one-dimensional strings within the lattice<sup>3</sup>. In other words, if we put line segments through each unhappy vertex connecting those plaquettes, as in Figure 2, and then attach the segments, we find that all the unhappy vertices can be represented as strings. These strings start and end in the interior plaquettes, because of the odd number of connecting vertices in those plaquettes. Since the strings represent purely topological constraints of the Santa Fe structure, the emergent string representation is valid at any temperature, although, at high enough temperatures, closed loop strings can also form. Notably, these strong one-dimensional string correlations among unhappy vertices at low temperatures contrast sharply with the unhappy vertices in other vertex-frustrated systems: Tetris ice has only weak correlations<sup>6,10</sup> and Shakti ice has algebraic correlations<sup>6,9,11,21</sup>. The strongly stringcorrelated unhappy vertices in SFI, by contrast, couple to become one-dimensional

collective emergent objects whose motion and evolution define the kinetics of the system. String correlations are familiar in quantum topological matter, a consequence of quantum entanglement<sup>22,23</sup>, but here they represent an unusual example of an emergent extended classical structure arising from the geometry of the lattice and the topology of the frustration.

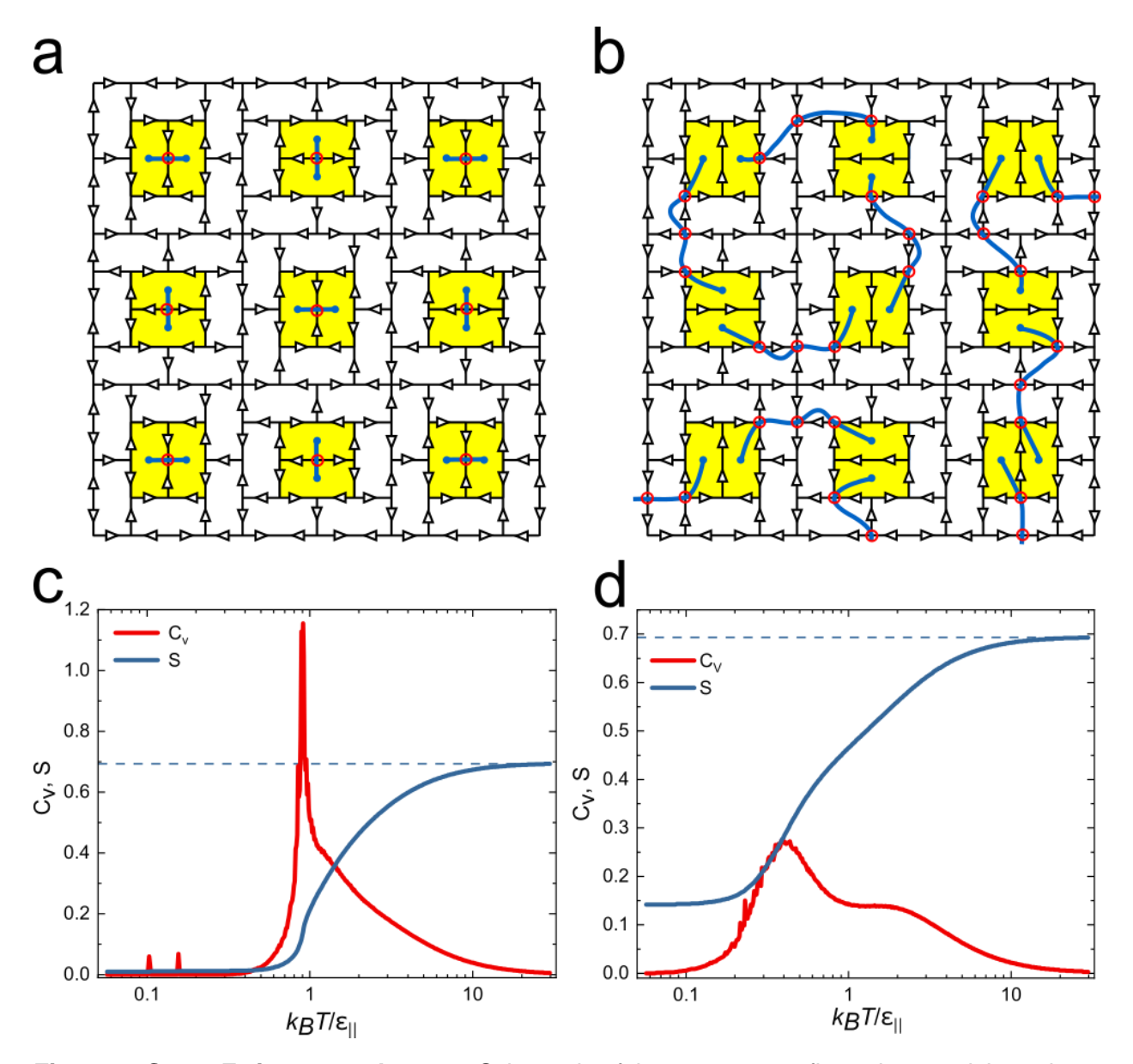


Figure 3: Santa Fe ice ground states. Schematic of the moment configurations and the strings, showing (a) the long-range-ordered ground state, and (b) the disordered string ground state. (c) and (d) specific heat ( $C_V$ ) and entropy (S) per moment as a function of effective temperature from Monte Carlo calculations for  $\Delta \epsilon_{II_3}/\Delta \epsilon_{II_2} = 0.9$  and 0.3, respectively (as described in the Supplementary Information). The simulations yield the long-range-ordered state and the disordered string ground state in these two cases. Note the sharp peak associated with the transition to long range order, the broad peak associated with the evolution to the disordered ground state, and the shoulder in each case associated with the development of short range order on the vertices. Note the residual entropy in the entropy curve for the disordered state. Entropy at infinite temperature is In2 (dashed blue line).

Within this string representation, it is straightforward to determine the second SFI collective ground state. Because they are made of unhappy vertices, by definition energetically excited, strings carry tensile strength. Thus, the ground state of the system corresponds to the least number of strings, each with the shortest possible length of three unhappy vertices, anchored in neighboring interior plaquettes (Figure 3b). Excited states above the ground state then correspond to longer strings that could potentially run between interior plaquettes that are not near neighbors. There is an extensively degenerate way to arrange strings in the ground state, leading to non-zero density of entropy. Indeed the *ground state* can be mapped into a dimer cover model, similar to the case of Shakti ice<sup>11</sup>, which can be used to calculate its entropy as discussed in the Supplementary Information.

For a given instantiation of SFI, which of the two possible ground states has a lower energy depends on the details of the interaction energies between neighboring island moments. Within a simple vertex model, i.e., ignoring interactions beyond those among islands sharing a vertex, the energetics of the two states can be compared by noting that the long-range-ordered ground state has a single Type II<sub>2</sub> unhappy vertex in place of three Type II<sub>3</sub> unhappy vertices in the disordered string ground state. Thus, in the context of such a vertex model, the ordered state is the ground state of the system when  $\epsilon_{II_2} - \epsilon_{I_2} < 3(\epsilon_{II_3} - \epsilon_{I_3})$  or  $\Delta \epsilon_{II_3}/\Delta \epsilon_{II_2} > 1/3$ , where  $\epsilon$  represents the energy of a vertex moment configuration. We have performed Monte Carlo simulations of SFI in order to better understand its behavior (details in Supplementary Information), and the results in Figure 3c and 3d show the calculated specific heat of the system evolving with decreasing effective temperature from a random paramagnetic state. There is a broad shoulder in both cases that corresponds to the vertices mostly entering their local ground states, and

then either a broad or a sharp peak associated with the system entering the disordered or ordered ground state, respectively. The non-zero residual entropy of the disordered string ground state is clearly visible in Figure 3d. We note that numerical simulations show that inclusion of longer range interactions can increase the crossover point between the states to higher values of  $\Delta\epsilon_{II_3}/\Delta\epsilon_{II_2}$ , so the vertex model estimate of  $\Delta\epsilon_{II_3}/\Delta\epsilon_{II_2}=1/3$  should be considered only as a rough estimate of where the crossover between the two ground states occurs, and the actual crossover may be higher (details of the calculations and additional results are given in the Supplementary Information).

We have experimentally studied permalloy (Ni<sub>80</sub>Fe<sub>20</sub>) SFI both in a static configuration after high temperature annealing and also in a dynamic state undergoing thermal moment reversals. In these two distinct cases, we image the moments through magnetic force microscopy (MFM) and photoemission electron microscopy (PEEM), respectively. Details of island size, lattice constant, sample fabrication and measurement protocols are given in the Methods section, and typical images of the moments for each technique are shown in Figures 1c and 1d. We note that micromagnetic calculations indicate that  $\Delta \epsilon_{II_3}/\Delta \epsilon_{II_2}$  is around 0.7 – 0.95 for the high temperature annealing samples and around 0.6 – 0.75 for the dynamic samples, with the differences arising from the different dimensions of the islands (see Supplementary Information for details).

The thermal annealing method is very efficient in reaching low energy states<sup>24,25,26</sup>, because it starts near the Curie point, where the material from which the nanoislands are formed is weakly ferromagnetic. Thus, the constraints predicated upon the binary nature of the island magnetization necessarily break down during this process. Figures 4a - 4c plot the fractions of the possible vertex moment configurations after high-temperature annealing, as a function of the lattice constant. The fractions converge close to the

predicted disordered string ground state values (fraction[I4] = 1, fraction[I3] =  $11/14 \sim 0.79$ , and fraction[II3] =  $3/14 \sim 0.21$ ) as the lattice constant is reduced and the moments become more strongly coupled. On close inspection, we observe occasional instances of interior plaquettes with only a single unhappy z = 2 vertex shared between them, and larger regions of the disordered string ground state, as shown in the moment maps of Figure 4d and 4e. These results suggest that the samples are situated near the boundary between the two ground states. Naturally, at larger lattice spacing, there is enhanced disorder associated with the weaker interactions and commensurately more complex string structures, as illustrated in Figure 4f.

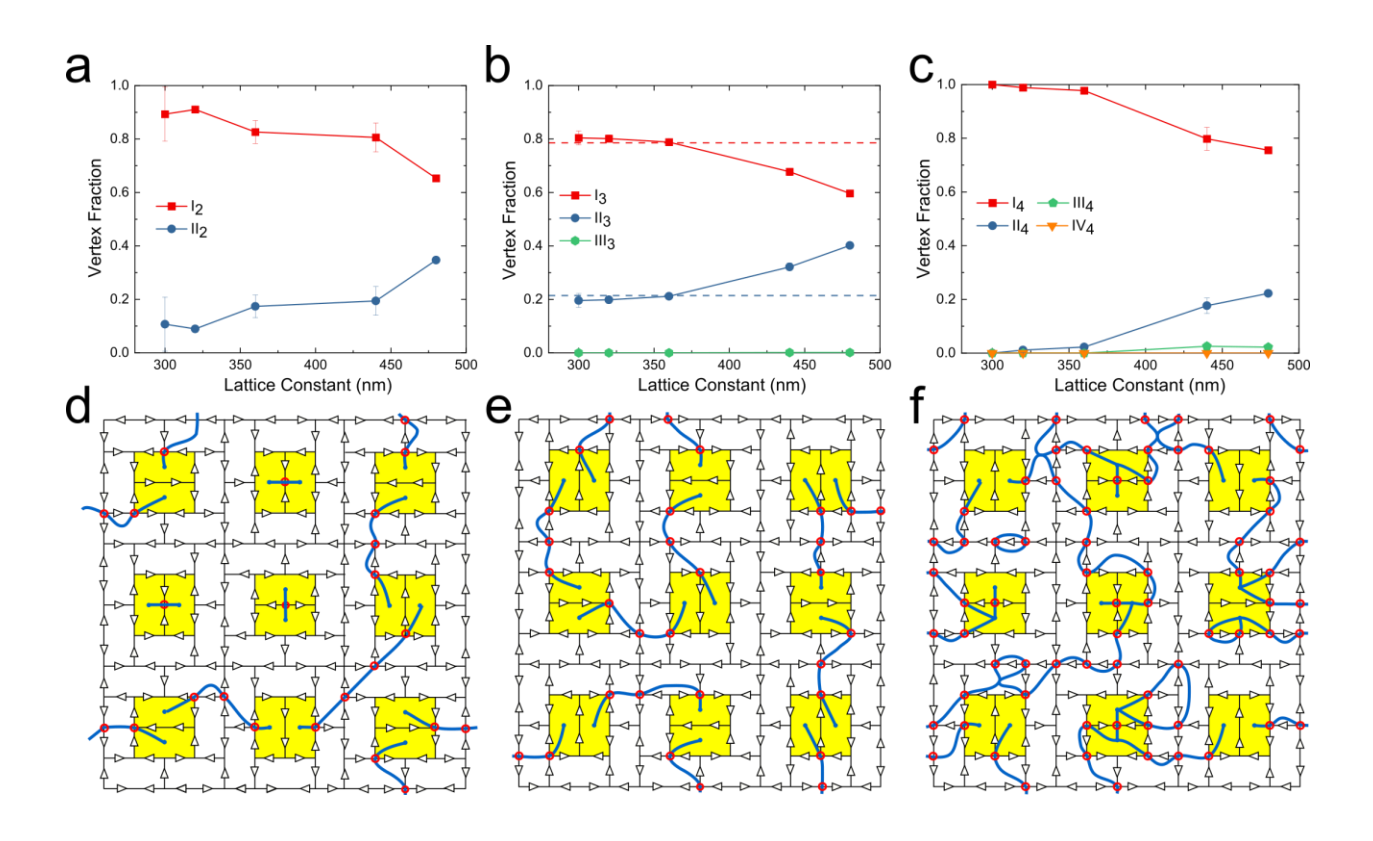
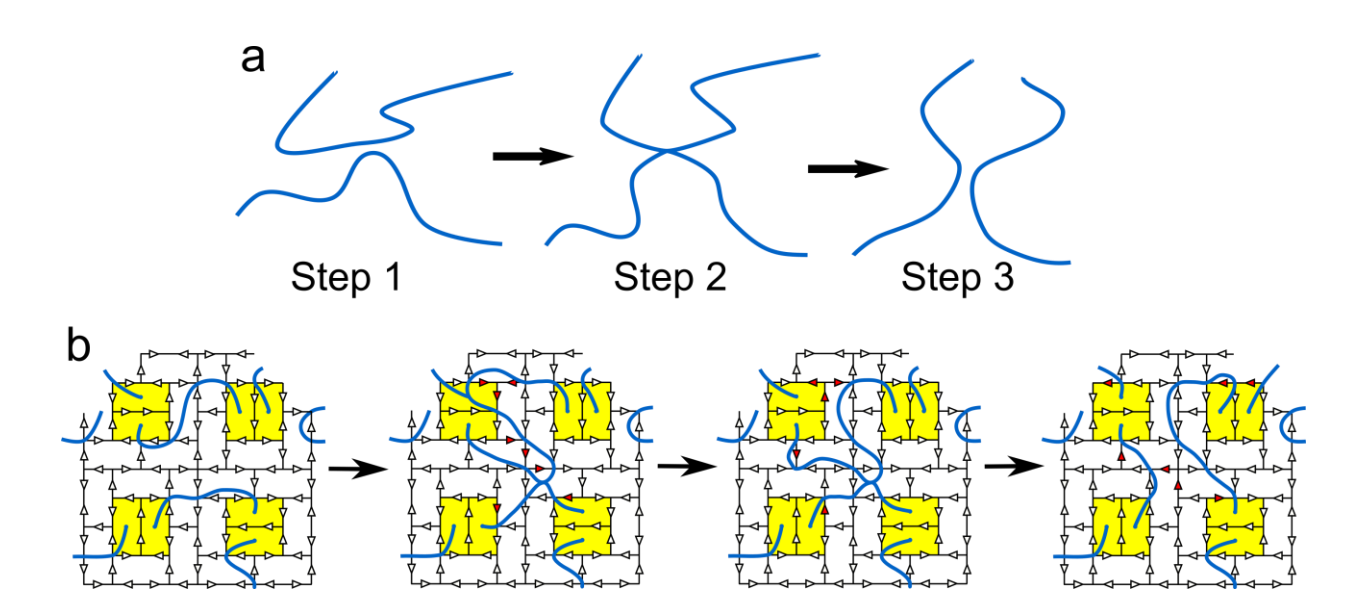


Figure 4: Thermal annealing results from MFM measurements (a-c) Vertex statistics after high temperature annealing as a function of lattice constant for different vertex coordination numbers, z = 2, 3, and 4, respectively. Dashed lines represent the predicted fraction of ground state vertices for z = 3. The data show that the system approaches that state as the coupling between islands increases with decreasing lattice constant. The error bars represent the standard deviation of vertex fraction that is extracted from MFM images taken from different locations and different runs. (d-f) Examples of moment configurations for small portions of the arrays measured after annealing, with both the moments and strings represented, showing the emergence of the long-range-ordered ground state (d), the disordered string ground state (e), and an excited state (f) configuration. The moment configurations were taken from MFM images of samples with lattice constants of 360 nm, 320 nm, and 480 nm respectively.

We now turn to the kinetics of SFI, as revealed by PEEM measurements of the moment configuration of SFI in a temperature regime where the individual moments are thermally active. This method differs from high-temperature annealing in that it probes the system in the limit where all islands have well-defined and fluctuating binary moments, and the moment configurations are therefore the result of discrete moment flips. To understand the consequences of such flip dynamics on the emergent strings, we note that the string representation of excitations allows us to partition the phase space of possible moment configurations into topological sectors for the strings. In other words, we can understand the string configurations in terms of homotopy classes, i.e., sets of configurations that are topologically equivalent in that they include all the ways the strings can be deformed without changing their ends.

Within this picture of homotopy classes, there are two possible types of kinetics. One is topologically trivial, the other non-trivial. The topologically trivial kinetics corresponds to fluctuations of the strings with the constraint that the ends of the strings cannot change. These kinetics thus do not change the homotopy class. In order to explore the full extent of phase space, however, the system needs to execute topologically non-trivial kinetics that cut across homotopy classes, i.e., change the way strings run between interior plaquettes. Importantly, the system needs to cut among homotopy classes in order to relax. Such changes in the moment configuration constitute a physical manifestation of one-dimensional "topological surgery" <sup>7, 27</sup>, where strings are effectively broken and reattached to each other in a new, topologically distinct configuration. This is easiest to visualize in the example of two strings elongating in a homotopic manner, and then crossing each other within a plaquette so that the choice of which string is which becomes ambiguous (see Figure 5a). They can then separate again, as two different strings with

different anchoring points, which are thus in a different homotopy class. Such "surgery" of cutting and reattaching is a direct mathematical analog of chromosome meiosis or DNA recombination, also described mathematically as topological surgery<sup>28</sup>.



**Figure 5: Topological surgery in SFI** (a) A schematic of topological surgery for strings of unhappy vertices. (b) Schematics of the PEEM images taken at 0.7 second time intervals (0.2 second exposure time and 0.5 second read-out time) with island moment and string representation, showing the process of topological surgery. These data are for SFI with a = 700 nm at 330 K during the second PEEM run (see Supplementary Information). The moments indicated by red arrow heads mark those that reversed direction relative to the previous frame. Broken lattice lines indicate that the islands were outside of the PEEM image boundary.

Our PEEM experimental temperature range extends from high temperatures, where all of the moments are thermally reversing at higher frequency than can be imaged, to temperatures at which the moments are virtually static on the time scale of the experiment (typically a range of about 100 K for our samples, with the exact range determined by the details of the island structure). Time sequences of PEEM images allow us to observe both the homotopic changes and topological surgery in SFI by tuning the temperature so that the moment reversal time scales are compatible with the time scale for imaging (this changes for different samples). As an example of the latter, Figure 5b shows sequentially measured moment configurations, taken from successive PEEM images at a temperature where the moments are fluctuating. The crossing, breaking, and reconfiguration of the strings is clear in these images, unambiguously demonstrating topological surgery.

Somewhat surprisingly, the PEEM results do not converge upon cooling to either the disordered string ground state or the long-range-ordered ground state. We extracted vertex statistics and the rate of island moment flipping from the images taken on cooling, and we plot typical data as a function of temperature in Figure 6. The temperature dependence of the vertex fractions is weak, although flip rates are fast compared to the data acquisition time, and the flip rates change by at least an order of magnitude in our temperature range, suggesting slow relaxation and retained memory. Notably, the vertex fractions are consistent across the lattice spacings in our fourth PEEM run, where we did a direct comparison of three different lattice spacings. That sample had the highest fluctuation rate at room temperature, and the data thus suggest that the topology of the lattice structure leads the system to be trapped in a specific metastable state in these

measurements. We note that the other samples do not vary much from those vertex fractions, supporting this conjecture (see Supplementary Information).

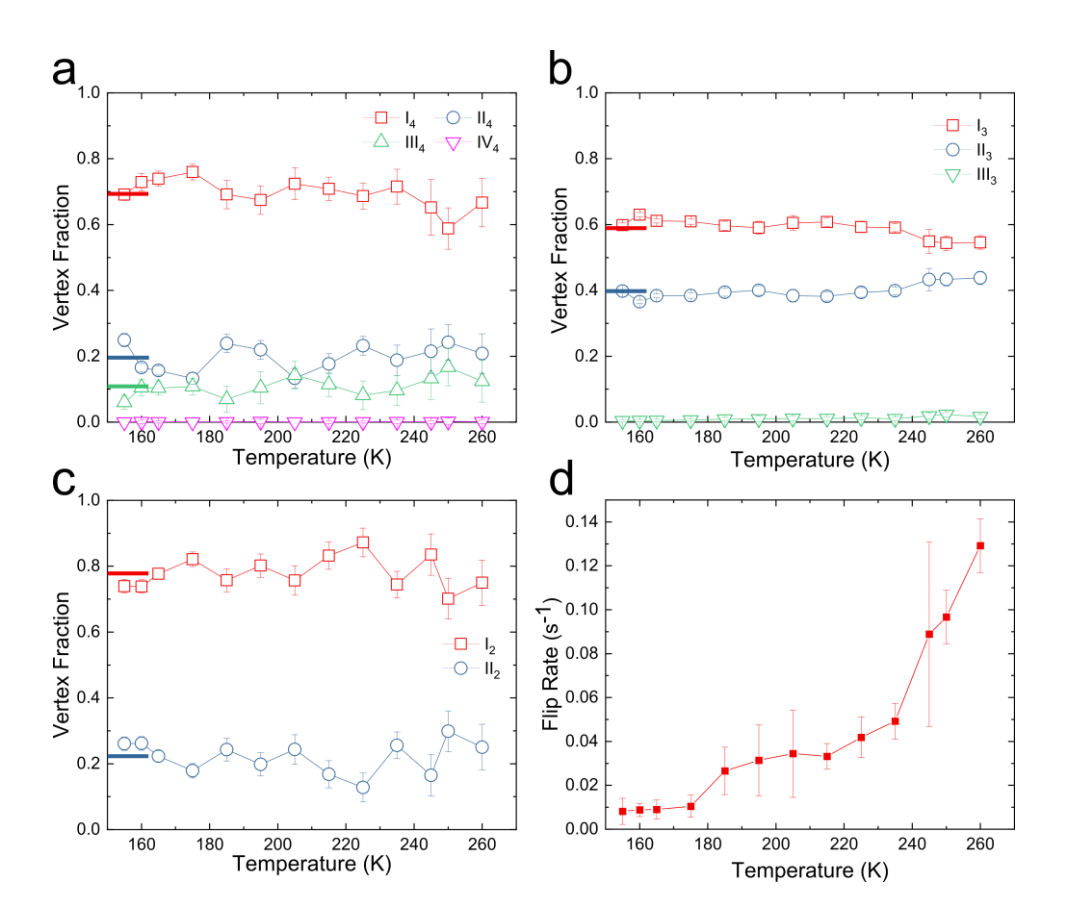


**Figure 6: Vertex statistics from PEEM data** (a-c) Vertex statistics for vertex coordination of z = 4, 3, and 2, respectively, as a function of temperature for PEEM data taken during the fourth PEEM run on SFI with a = 800 nm, with data acquisition for 150 seconds at each temperature. The segments on the left mark average vertex fraction for given types. (d) The average island moment flip rate as a function of temperature extracted from the same PEEM data set. The error bars in all frames reflect the standard deviation of the data taken from all (100) PEEM images at the given temperature.

We can understand the trapping of the system in a metastable state as the kinetic suppression of topological surgery, since, for the system to reach either ground state through discrete moment flips, topological surgery must be performed. To achieve the

long-range-ordered ground state, for example, loop-like strings must be created that run between pairs of interior plaquettes that share a boundary, which then can be contracted to the desired Type-II<sub>2</sub> vertex. In order to create such loop-like strings from strings that run between separated interior plaquettes, the system must undergo topological surgery that simultaneously creates a longer string between more distant interior plaquettes. This process cannot occur without creating Type III<sub>4</sub> vertices, which requires overcoming a significant local energy barrier, and thus this process is strongly suppressed at low temperature.

Our Monte Carlo simulations, with varying assumptions about the relative near neighbor interactions, i.e., the ratio  $\Delta \epsilon_{II_3}/\Delta \epsilon_{II_2}$ , further elucidate the physics involved (detailed data in Supplementary Information). When the system is expected to have an ordered state, the simulations show that it is reached via a non-monotonic path in the vertex fractions. For values of  $\Delta\epsilon_{II_3}/\Delta\epsilon_{II_2}$  much higher than the crossover threshold for ordering, the system approaches the disordered string ground state upon cooling, before evolving to the long-range-ordered state. The non-monotonicity is most easily seen as a local minimum in the Type II<sub>2</sub> population as a function of temperature. For values of  $\Delta\epsilon_{II_3}/\Delta\epsilon_{II_2}$  close to the crossover value, the system remains trapped in that minimum, corresponding to an (excited) disordered string state, and fails to reach order in the longest simulations attempted. This lack of equilibration, elucidated in detail in the Supplementary Information, is strongly suggestive of what we see in the experimental PEEM results, and suggests a natural kinetic trap into which the system might fall, since topological surgery is required for the system to escape that minimum. Significantly, the Monte Carlo simulations mirror the individual moment-flipping kinetics of our PEEM experiments, albeit with simplified energetics, a much smaller system size, and much longer time scale, all of which should allow better equilibration than accessible experimentally. That the simulation results clearly show a lack of equilibration into the ground state is strongly suggestive that the magnetic system is unable to equilibrate in the context of the required but kinetically improbable topological surgeries.

Given the unusual dynamics associated with the string excitations in SFI, the natural next questions will be how the strings will affect other phenomena, such as the macroscopic magnetization and hysteretic memory effects, and how generalizable our observed kinetically constrained topological surgery might be to other lattice structures and other types of interactions. The classification of the low energy state of a system in terms of homotopy classes for an emergent string and loop picture is familiar in quantum matter, for instance in braiding of anyons or topological degeneracy in spin liquids<sup>22,29,30</sup>. While such long-range quantum entanglement is absent in classical materials, the observed behavior of SFI demonstrates that frustration can impose strict rules on disorder, from which a phase of strings as topological objects will emerge. In classical systems, such topological order is known to affect the kinetics,<sup>31,32</sup> which evolve through rupture of the topological protection. An analogous quantum system, comprised of interacting qubits rather than classical moments, is a clear aspirational goal for this sort of structure.

Importantly, our data provide an experimental manifestation of a system with weak structural disorder, in which a topologically complex state can arise strictly from the frustrated geometry, and furthermore in which the path to a ground state is explicitly impeded by the requirement for topological surgery. The approach to ordering is outside the Landau paradigm and points to the need for a novel theoretical framework with which to understand phase transitions between well-defined topological states and long-range

order. Artificial spin ice systems, being both designable and unusually open to different experimental probes at the constituent level, are uniquely suited to developing such a framework in a classical context. Further probes of these systems should open the door to the equivalent analysis in the realm of quantum systems, from which we can clearly anticipate further unexpected phenomena.

## **METHODS**

The artificial spin ice samples used in this work were fabricated through a process similar to that described in previous papers<sup>9,10,11,13</sup>. We used electron-beam lithography to write the patterns on silicon substrates with spin-coated bilayer resists. Various thicknesses of permalloy films were then deposited into the patterns, followed by 2-3 nm aluminum capping layers to prevent oxidation of the underlying permalloy.

The samples used for thermal annealing experiments had lateral island dimensions of 220 nm × 80 nm and thickness of 15 nm. These dimensions were chosen so that the magnetic moments of the nanoislands were frozen at room temperature. Five SFI arrays were designed with lattice constants of 300 nm, 320 nm, 360 nm, 440 nm, and 480 nm. All arrays were polarized along the [1,1] direction, then heated to 818 K at a rate of 10 K/min. The samples were held at 818 K for 15 minutes before being cooled to 673 K at a rate of 1 K/min and then to room temperature. Two MFM scans were performed on each array to minimize location variances. Each MFM image contained about 900 total vertices and 1500 moments. Square ice lattices that were annealed simultaneously showed large ground state domains in MFM scans, demonstrating that the annealing protocols used could successfully set vertices to the low energy states.

We conducted four runs of PEEM experiments at the PEEM 3 endstation of the Advanced Light Source, Lawrence Berkeley National Lab. The samples used for the PEEM experiments had lattice constant of 600 nm, 700 nm, and 800 nm and islands with lateral dimensions of 470 nm x 170 nm. The permalloy thicknesses of PEEM samples were approximately 2.5 nm, and the island moments were thermally active in the tested temperature window. Note that samples fabricated for different PEEM experiments had variable temperature windows for thermally active islands, due to the 5-10% thickness uncertainty in deposition. For the first, second, and fourth PEEM run, we focused on dynamics, taking a series of 100 PEEM images at each temperature point as samples were heated or cooled. The 100 PEEM images consisted of ten exposures with a leftcircularly polarized X-ray beam followed by ten exposures with a right-circularly polarized beam, repeated five times. The exposure time was set to 0.2 to 0.5 seconds and the total acquisition time at each temperature was about 130 to 150 seconds including computer read-out between exposures. The island flip rate was obtained by calculating the fraction of islands that changed their moment directions between two sequential PEEM images taken at each temperature, divided by the acquisition time of two images. For the third PEEM run, we took two PEEM-XMCD images at 10 different locations at each temperature point to obtain better statistics. Each image was constructed from four PEEM images with a left-polarized X-ray beam and four with a right-polarized beam; we took the average of every four images and subtracted the images with left-polarized X-rays from the right-polarized X-rays to obtain a PEEM-XMCD image. The exposure time for each image was 0.7 seconds for better image resolution. Besides the data shown in Fig 6, other PEEM measurements and detailed associated parameters can be found in Supplementary Information.

## **AUTHORS' CONTRIBUTIONS**

J. Batley and J. D. Watts performed film depositions under the guidance of C. Leighton, and D. Bromley prepared other samples under the guidance of L. O'Brien, with X. Zhang, Y. Lao, J. Sklenar, and N. S. Bingham overseeing the lithography. X. Zhang, Y. Lao, J. Sklenar, N. S. Bingham and H. Saglam performed the PEEM characterization of the thermally active samples under the guidance of P. Schiffer. X. Zhang and N. S. Bingham performed above-Curie point annealing and MFM characterization under the guidance of P. Schiffer. X. Zhang and H. Saglam performed micromagnetic calculations under the guidance of P. Schiffer. A. Duzgun performed Monte Carlo and spin dynamics simulations, under the guidance of C. Nisoli. C. Nisoli provided the string picture of the ground state and kinetics and wrote the first draft. P. Schiffer supervised the entire project. All authors contributed to the discussion of results and to the finalization of the manuscript.

#### FUNDING ACKNOWLEDGEMENT

Work at Yale University and the University of Illinois at Urbana-Champaign was funded by the US Department of Energy, Office of Basic Energy Sciences, Materials Sciences and Engineering Division under Grant No. DE-SC0010778 and Grant No. DE-SC0020162. This research used resources of the Advanced Light Source, a DOE Office of Science User Facility under contract no. DE-AC02-05CH11231. Work at the University of Minnesota was supported by NSF through Grant No. DMR-1807124. Work

at the University of Liverpool was supported by the UK Royal Society, Grant No. RGS\R2\180208. The work of C.N. was carried out under the auspices of the US DoE through LANL, operated by Triad National Security, LLC (Contract No. 892333218NCA000001) and financed by DoE LDRD.

# DATA AVAILABILITY

Experimental and simulation data are available from the authors upon request.

# **REFERENCES**

<sup>&</sup>lt;sup>1</sup> R. F. Wang, C. Nisoli, R. S. Freitas, J. Li, W. McConville, B. J. Cooley, M. S. Lund, N. Samarth, C. Leighton, V. H. Crespi, and P. Schiffer, Nature **439**, 303 (2006).

<sup>&</sup>lt;sup>2</sup> I. Gilbert, C. Nisoli, and P. Schiffer, Physics Today **69**, 54 (2016).

<sup>&</sup>lt;sup>3</sup> C. Nisoli, V. Kapaklis, and P. Schiffer, Nature Physics **13**, 200 (2017).

<sup>&</sup>lt;sup>4</sup> N. Rougemaille, B. Canals, European Physical Journal B **92**, 62 (2019).

<sup>&</sup>lt;sup>5</sup> S. H. Skjærvø, C. H. Marrows, R. L. Stamps, and L. J. Heyderman, Nature Reviews Physics **2** 13 (2020).

<sup>&</sup>lt;sup>6</sup> M. J. Morrison, T. R. Nelson, and C. Nisoli, New Journal of Physics 15, 045009 (2013).

<sup>&</sup>lt;sup>7</sup> J. W. Milnor, in *Proc. Sympos. Pure Math.* **3**, 39 *AMS* (1962).

<sup>&</sup>lt;sup>8</sup> M. Harris, S. Bramwell, D. McMorrow, T. Zeiske, and K. Godfrey, Physical Review Letters **79**, 2554 (1997).

<sup>9</sup> I. Gilbert, G.-W. Chern, S. Zhang, L. O'Brien, B. Fore, C. Nisoli, and P. Schiffer, Nature Physics **10**, 670 (2014).

<sup>10</sup> I. Gilbert, Y. Lao, I. Carrasquillo, L. O'Brien, J. D. Watts, M. Manno, C. Leighton, A. Scholl, C. Nisoli, and P. Schiffer, Nature Physics **12**, 162 (2016).

<sup>11</sup> Y. Lao, F. Caravelli, M. Sheikh, J. Sklenar, D. Gardeazabal, J. D. Watts, A. M. Albrecht, A. Scholl, K. Dahmen, C. Nisoli, and P. Schiffer, Nature Physics **14**, 723 (2018).

<sup>12</sup> S. Gliga, G. Hrkac, C. Donnelly, J. Büchi, A. Kleibert, J. Cui, A. Farhan, E. Kirk, R. V. Chopdekar, Y. Masaki, N. S. Bingham, A. Scholl, R. L. Stamps and L. J. Heyderman, Nature Materials **16**, 1106 (2017).

<sup>13</sup> J. Sklenar, Y. Lao, A. Albrecht, J. D. Watts, C. Nisoli, G.-W. Chern, and P. Schiffer, Nature Physics **15**, 191 (2019).

<sup>14</sup> D. Louis, D. Lacour, M. Hehn, V. Lomakin, T. Hauet, and F. Montaigne, Nature Materials **17**, 1076 (2018).

<sup>15</sup> D. Shi, Z. Budrikis, A. Stein, S. A. Morley, P. D. Olmsted, G. Burnell, and C. H. Marrows, Nature Physics **14**, 309 (2018).

<sup>16</sup> N. Leo, S. Holenstein, D. Schildknecht, O. Sendetskyi, H. Luetkens, P. M. Derlet, V. Scagnoli, D. Lançon, J. R. Mardegan, T. Prokscha, et al., Nature Communications 9, 2850 (2018).

<sup>17</sup> Y.-L. Wang, Z.-L. Xiao, A. Snezhko, J. Xu, L. E. Ocola, R. Divan, J. E. Pearson, G. W. Crabtree, W.-K. Kwok Science **352**, 962 (2016).

<sup>18</sup> A. Farhan, C. F. Petersen, S. Dhuey, L. Anghinolfi, Q. H. Qin, M. Saccone, S. Velten, C. Wuth, S. Gliga, P.Mellado, M. J. Alava, A. Scholl, S. van Dijken, Nature Communications 8, 995 (2017).

<sup>19</sup> R. Baxter, Exactly solved models in statistical mechanics (Academic, New York, 1982).

<sup>20</sup> Robert L. Stamps, Nature Physics **10**, 623 (2014)

<sup>21</sup> G.-W. Chern, M. J. Morrison, and C. Nisoli, Physics Review Letters 111, 177201 (2013).

<sup>22</sup> Michael A. Levin and Xiao-Gang Wen, Physical Review B **71**, 045110 (2005).

<sup>23</sup> A. Kitaev, Annals of Physics, **321**, 2 (2006).

<sup>24</sup> S. Zhang, I. Gilbert, C. Nisoli, G.-W. Chern, M. J. Erickson, L. O'Brien, C. Leighton, P. E. Lammert, V. H. Crespi, and P. Schiffer, Nature **500**, 553 (2013).

<sup>25</sup> J. Porro, A. Bedoya-Pinto, A. Berger, and P. Vavassori, New Journal of Physics **15**, 055012 (2013).

<sup>26</sup> X. Zhang, Y. Lao, J. Sklenar, N. S. Bingham, J. T. Batley, J. D. Watts, C. Nisoli, C. Leighton, P. Schiffer, APL Materials **7**, 111112 (2019).

<sup>27</sup> M. Marino, Reviews of Modern Physics **77**, 675 (2005).

<sup>28</sup> S. Antoniou and S. Lambropoulou, PloS One **12**, e0183993 (2017).

<sup>29</sup> F. Wilczek, Quantum Mechanics of Fractional-Spin Particles. Physical Review Letters **48**, 114, (1982).

<sup>30</sup> T. Lan, J. C. Wang, and X.-G. Wen, Physical Review Letters **114**, 076402 (2015).

<sup>31</sup> C. L. Henley, Christopher L. Journal of Physics: Condensed Matter 23, 164212 (2011).

<sup>32</sup> R. Z. Lamberty, S. Papanikolaou, and C. L. Henley. Physical Review Letters **111**, 245701 (2013).